

Incorporating Lithium-Deficient Layer and Interfacial-Confined Catalysis Enables the Reversible Redox of Surface Oxygen Species in Lithium-Rich Manganese-based Oxides

Supporting Information

Junpeng Sun,^a Hai Yang,^a Jialong Shen,^a Huadong Qi,^a Mei Sun,^b Yuhang Lou,^a Yu Yao,^a Xianhong Rui,^c Yu Shao,^d Xiaojun Wu,^a and Yan Yu*^a

^aHefei National Research Center for Physical Sciences at the Microscale, Department of Materials Science and Engineering, iChEM (Collaborative Innovation Center of Chemistry for Energy Materials), CAS Key Laboratory of Materials for Energy Conversion, University of Science and Technology of China, Hefei, Anhui, China

Email: yanyumse@ustc.edu.cn

^bInstruments Center for Physical Science, University of Science and Technology of China, Hefei, Anhui, China

^cSchool of Materials and Energy, Guangdong University of Technology, Guangzhou, 510006, China

^dJiujiang DeFu Technology Co. Ltd., Jiujiang, Jiangxi, China

Preparation of Cathode Materials

All the reagents were purchased from Sigma Aldrich and were used without further purification. The carbonate precursors were synthesized by the co-precipitation method. $\text{Mn}(\text{CH}_3\text{COO})_2 \cdot 4\text{H}_2\text{O}$, $\text{Ni}(\text{CH}_3\text{COO})_2 \cdot 4\text{H}_2\text{O}$, and $\text{Co}(\text{CH}_3\text{COO})_2 \cdot 4\text{H}_2\text{O}$ were dissolved in 100 mL of ethylene glycol according to a molar ratio of 0.56: 0.16: 0.08. Subsequently, 2 g of polyvinyl pyrrolidone (PVP, K30) was added to the solution, and the mixture was stirred for 1 hour to obtain Solution A. NH_4HCO_3 was dissolved in 40 mL of deionized water to prepare Solution B. Solution B was then added into solution A dropwise. The mixture was continuously stirred for 180 minutes and then subsequently filtered. The prepared carbonate precursors were washed three times with deionized water and ethanol, respectively. Finally, the precursors were transferred to a vacuum oven at 120 °C and dried overnight.

1 g of the aforementioned carbonate precursor was mixed with stoichiometric amounts of lithium hydroxide, evenly spread on an alumina crucible, and positioned at the center of a muffle furnace. The mixture was calcinated at 800 °C for 12 hours, with a temperature ramp rate of 2 °C min^{-1} , to obtain the pristine sample.

To prepare the RuO_2 -coated samples, designated as Ru-0.5, Ru-1, and Ru-3, the pristine LRMO powder was immersed into 20 mL of RuCl_3 at concentrations of 0.1, 0.2, and 0.6 mg mL^{-1} . Following a 30-minute ultrasonic treatment, the solution was heated to 60 °C and stirred continuously until it was dried. The resulting mixture was collected and washed with deionized water to remove the residual Cl^- , and then dried in a vacuum oven. The dried powder was subsequently calcinated at 450 °C for 3 hours.

Electrochemical Tests

The electrochemical properties were evaluated using CR2032 coin cells. To prepare the LRMO electrode, the LRMO powder was mixed with Super P and PVDF in a weight ratio of 8:1:1, and dissolved in a proper amount of N-Methyl-2-pyrrolidone (NMP). The resulting slurry was coated onto aluminium foil and subsequently dried in a vacuum oven at 120 °C for over 12 h, achieving a mass loading of about 2.0 mg cm^{-2} . For the assembly of CR2032 coin cells, the coated foil was cut into disks measuring 12 mm in diameter. The counter electrode was Li foil, while the electrolyte consisted of 1 M LiPF_6 in EC and EMC (3:7 in volume ratio), sourced from Duoduo Company. The separator used was Celgard 2400.

All the pouch cell assembling processes were conducted in a dry room with a dew point lower than $-45\text{ }^{\circ}\text{C}$. The Ru-1 slurry was composed of 95 wt.% Ru-1, 2.5 wt.% Super P, 0.5 wt.% carbon nanotubes, and 2 wt.% polyvinylidene fluoride, using N-methyl-2-pyrrolidone (NMP) as the solvent. The solid content is about 55%. Then Ru-1 electrode for pouch batteries was fabricated by coating the aforementioned slurry on an aluminium foil. A Ru-1||graphite pouch cell was prepared by stacking the Ru-1 cathodes and graphite anodes (95 wt.% graphite). The mass loading of Ru-1 is 9 mg cm^{-2} and the N/P ratio is controlled at 1.05 in the pouch cell. Ru-1||Li pouch cells are fabricated by stacking the Ru-1 cathodes and lithium metal anodes. The electrolyte used was 1 M LiPF_6 in EC and EMC (3:7 in volume ratio), sourced from Duoduo Company. The electrolyte injection processes were conducted in an Argon-filled glovebox (H_2O and $\text{O}_2 < 0.1\text{ ppm}$). The pouch cell was activated between 4.75 to 2.0 V for the first cycle, and the corresponding charge and discharge curves are shown in Figure 3g.

The cycling tests were performed on Neware battery test system (CT-4008T-5 V10 mA-164, CT-4008T-5 V20 mA-164, Shenzhen, China) at room temperature. The CV tests were conducted on a CHI660D electrochemical workstation. Electrochemical Impedance Spectroscopy (EIS) measurements were conducted on CHI 660D electrochemical workstation and in the frequency from 0.01 Hz to 100 kHz.

Gas evolution was monitored using differential electrochemical mass spectrometry (DEMS) from Hiden Company. The DEMS in-situ cell was assembled within an argon-filled glovebox, utilizing a lithium metal strip as the anode and a Celgard 2400 membrane as the separator.

Structural characterization

The crystallographic structures of the respective samples were examined through X-ray diffraction (XRD) from Rigaku IV, utilizing $\text{Cu-K}\alpha$ radiation at 40 kV, 40 mA. The data were collected between diffraction angles (2θ) from 10° to 80° at a scan rate of 2° per minute. Rietveld refinements of the XRD patterns obtained by GSAS + EXPGUI suite. The ICP-AES tests were conducted on iCAP 7400, Thermo Fisher. The morphologies of different samples were scrutinized using a scanning electron microscope (CIQTEK SEM3100, GeminiSEM450). The high-resolution transmission electron microscopy (HRTEM) and energy dispersive spectrometer (EDS) images were collected from JSM-6700 of JEOL, Japan. The spherical aberration-corrected high-angle annular dark-field scanning transmission electron microscopy (HAADF-STEM) images and

electron energy loss spectroscopy (EELS) data were collected from Themis Z, Thermal Fisher. Raman analysis was conducted with Renishaw Via-Reflex Raman microscope. For in-situ surface-enhanced Raman scattering (SERS) spectroscopy tests, a proper amount of the suspension of the shell-isolated gold nanoparticles was dropped on the surface of the electrode. X-ray Absorption Spectroscopy (XAS) measurement performed in Total Electron Yield (TEY) mode, often captures signals from a depth of approximately 5 nm from the surface. In congruence, the probing depth of XPS measurement typically does not exceed 10 nm. Consequently, to sidestep the surface deposition layer and glean insights into the oxidation state of the bulk lattice oxygen, argon ion etching is employed to remove the oxide deposits from the electrode surface, with an etching depth of approximately 20 nm. The O K-edge and Ni, Co, and Mn L-edge data were recorded on Beamlines MCD-A and MCD-B (Soochow Beamline for Energy Materials) at the National Synchrotron Radiation Laboratory (NSRL). X-ray photoelectron spectroscopy (XPS) analysis was conducted on Kratos AXIS SUPRA+.

COMSOL

The Finite Element Method (FEM) is used to numerically solve the coupled partial differential equations of diffusion and mechanics, as implemented in the COMSOL Multiphysics. A three-dimensional electric field and ion distribution model was established using COMSOL to elucidate the ion distribution in different structures, coupled with solid mechanics to calculate stresses due to the uneven delithiation process. Given the complex nature of three-dimensional materials, the model was simplified to study Li^+ diffusion behaviour within the positive electrode particles. The model calculated the tendency of lithium ions to diffuse outward from the central sphere.

Stress in primary particle. In the parameter settings for the physical fields, a lithium-ion battery module was used to set the conductivity and volume fraction of the electrode material, allowing for the calculation of voltage and current distributions during the charging process. The dilute material transfer model was adopted, with Li^+ diffusion coefficients in LRMO set to $5 \times 10^{-10} \text{ cm}^2 \text{ s}^{-1}$. The solid mechanics module was employed to analyze the diffusion stress resulting from changes in the concentration of the negative electrode material during charging. The Young's modulus was set to 150 GPa, and the Poisson's ratio was set to 0.3.

O_2 diffusion. A three-dimensional model of oxygen diffusion was developed using COMSOL Multiphysics. The control model consisted of a sphere with a radius of 0.4 mm, while the

experimental model included a sphere with a radius of 0.38 mm enveloped by a 0.02 mm thick shell. The study employed the dilute species transport model, with the oxygen diffusion coefficient set at $1 \times 10^{-7} \text{ cm}^2 \text{ s}^{-1}$. Boundary conditions for the control model were defined as convection diffusion with a bulk concentration of zero. In contrast, the experimental model featured convection-diffusion boundary conditions with a bulk concentration that varied over time.

Computational Details

All the Density functional theory (DFT) calculations were conducted with the Vienna ab initio simulation package (VASP). The Perdew Burke Ernzerhof (PBE) functional within the generalized gradient approximation (GGA) was used to describe the exchange–correlation term.¹ The Projector Augmented Wave (PAW) method was applied to treat core electrons.² The cut-off energy was set as 520 eV, and the convergence criteria were set as 1×10^{-6} eV for energy and $0.02 \text{ eV } \text{Å}^{-1}$ for forces. In addition, spin-polarized and DFT + U methods were considered during the calculation.³ The U values for Mn and Ru are 3.9 and 4.88 eV, respectively.⁴ The migration energy barriers of Li atoms were evaluated by climbing-image nudged elastic band (cNEB) method.⁵ To better describe the interaction between adsorbate and substrate, Grimme’s method (DFT-D3) was employed in the surface adsorption calculations.

We constructed a $2 \times 1 \times 2$ Li_2MnO_3 supercell and then gradually replaced Li atoms in the TM layer with Mn atoms to obtain structures with different lithium contents. RuO_2 {001} and Li_2MnO_3 {003} surfaces were used to study the adsorption behaviour, and the vacuum region of 15 Å was set in the z direction to avoid interference between adjacent layers.

The adsorption energies were calculated by:

$$E_{ads} = E_{AB} - E_A - E_B$$

where E_{A+B} is the total energy of the adsorbed substrate, E_A is the total energy of the adsorbate, and E_B is the total energy of the substrate.

The Gibbs free energies were calculated by:

$$G = E_H + E_{ZPE} - TS$$

where E_H , E_{ZPE} and S are the total energy, the zero-point vibration energy and the entropy of the system, respectively.

Supplementary Figures

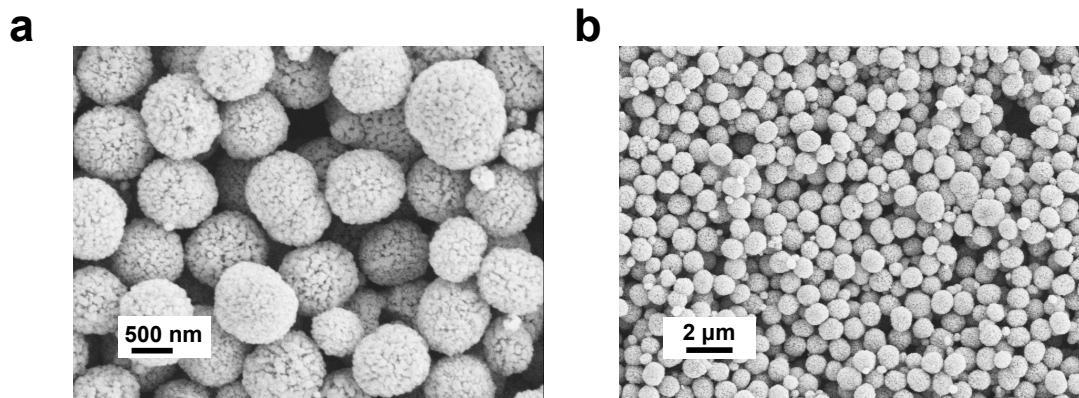


Figure S1 SEM images of the synthesized LRMO powder.

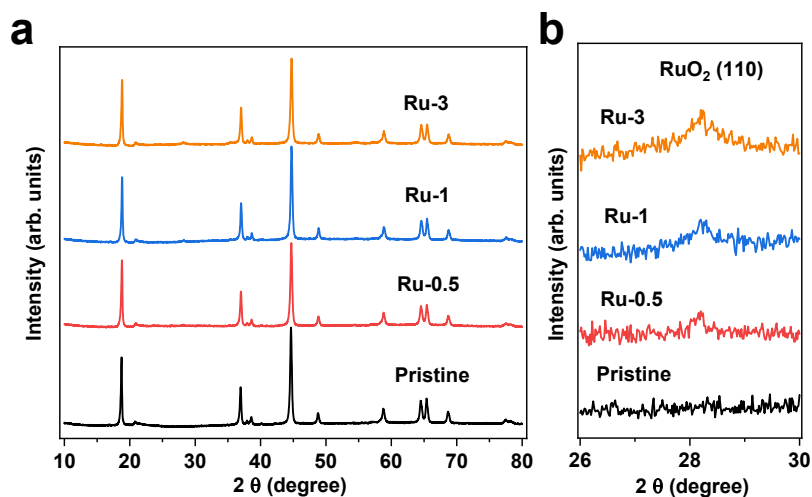


Figure S2 (a) XRD patterns of pristine sample, Ru-0.5, Ru-1, and Ru-3. (b) RuO₂ (110) peaks in pristine sample, Ru-0.5, Ru-1, and Ru-3.

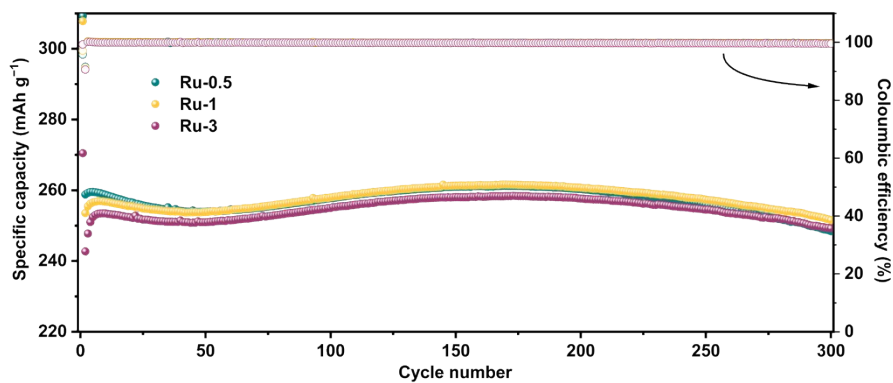


Figure S3 Long-term cycling performance of Ru-0.5, Ru-1, and Ru-3 at 1 C.

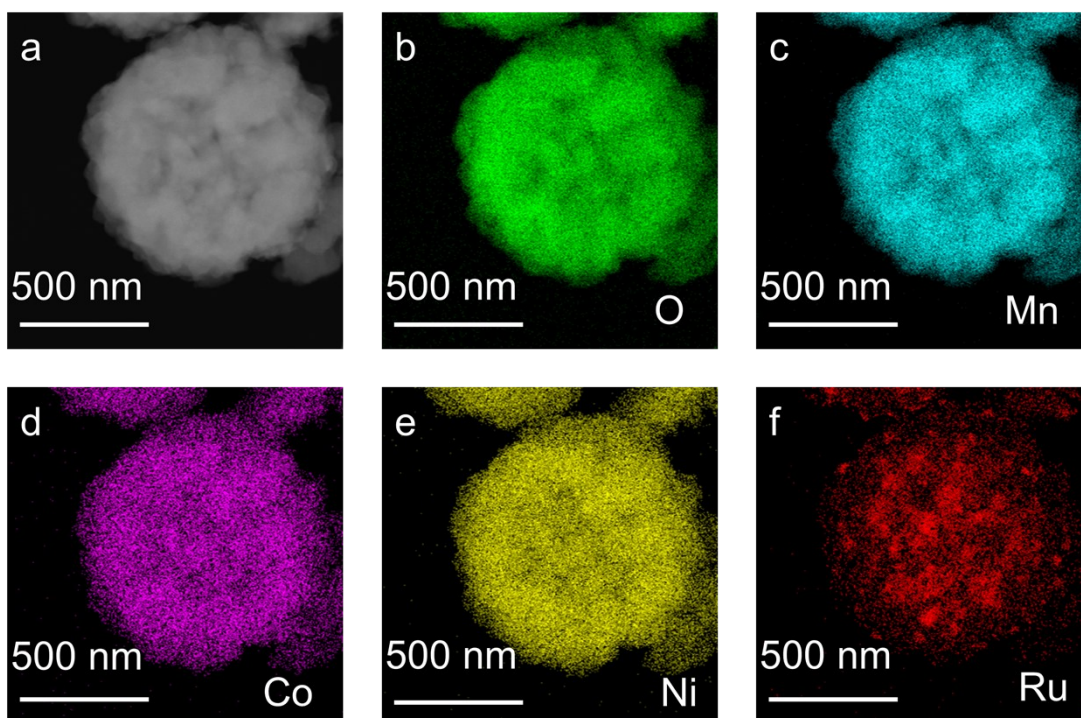


Figure S4 TEM EDS mapping images of Ru-1. (a) STEM image of Ru-1. Elements distribution of (b) O, (c) Mn, (d) Co, (e) Ni, and (f) Ru.

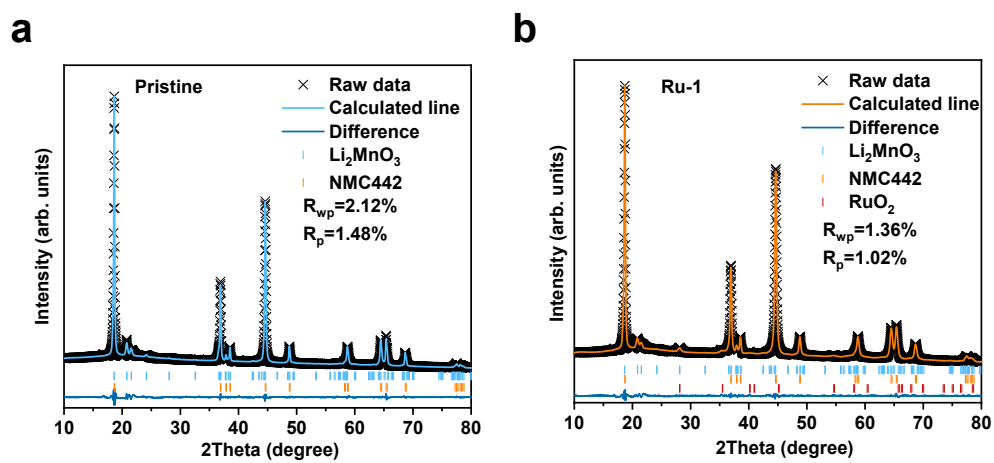


Figure S5 XRD refinement results of (a) pristine sample and (b) Ru-1.

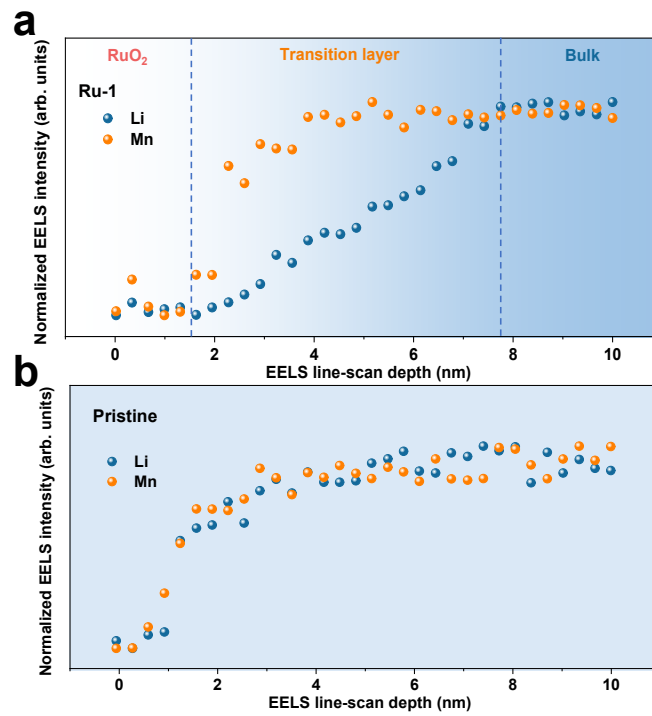


Figure S6 Line-scan EELS signal without fitting treatment of (a) Ru-1 and (b) Pristine sample.

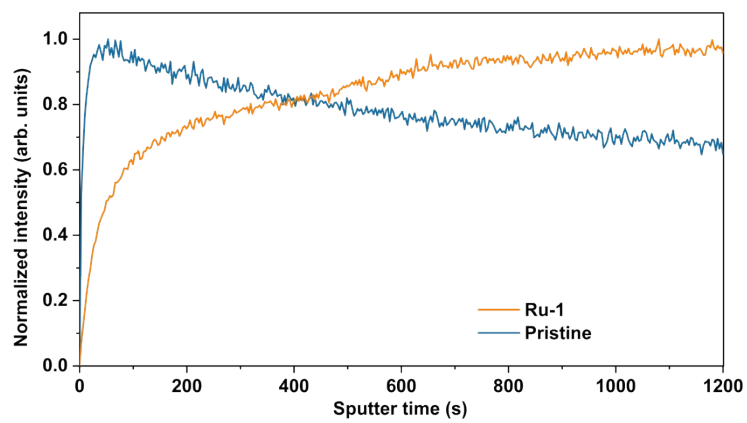


Figure S7 1D TOF-SIMS etching plots of Li signals of pristine sample and Ru-1.

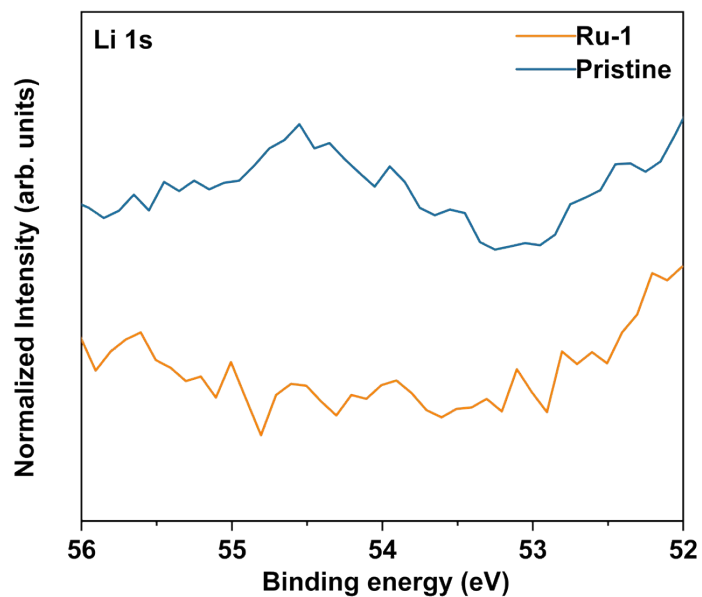


Figure S8 XPS spectra of pristine sample and Ru-1.

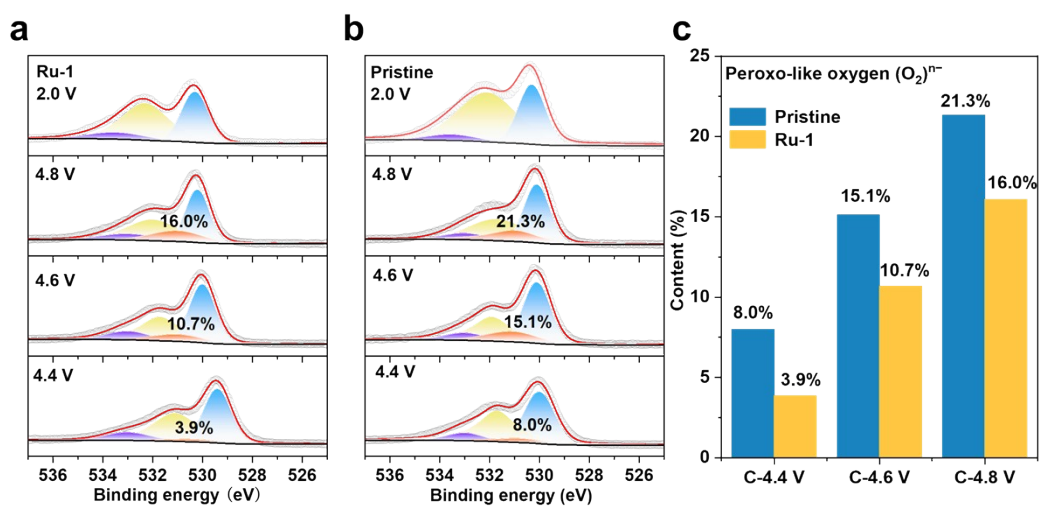


Figure S9 XPS spectra of (a) pristine sample and (b) Ru-1 at 4.4 V, 4.6 V, 4.8 V, and 2.0 V during the first charge and discharge process. (c) The corresponding content of peroxo-like oxygen.

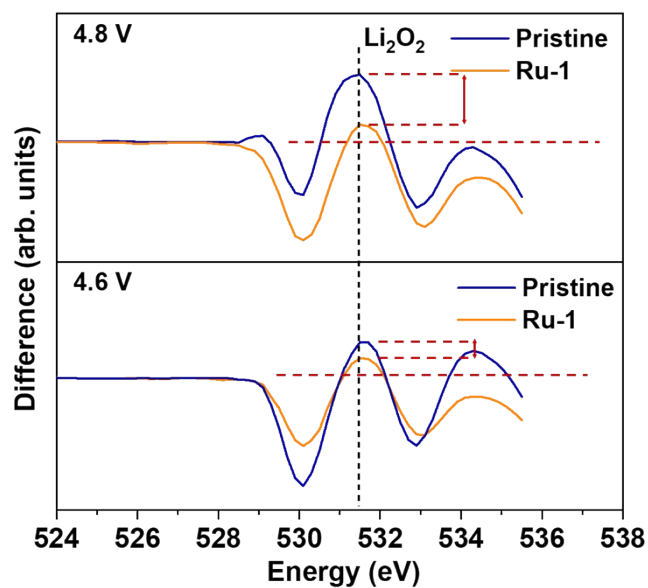


Figure S10 The difference of O K-edge sXAS spectra between 4.6/4.8 V and OCV during the initial charge process for Ru-1 and pristine samples. (Difference= (signal of 4.6 V or 4.8 V) – (signal of OCV))

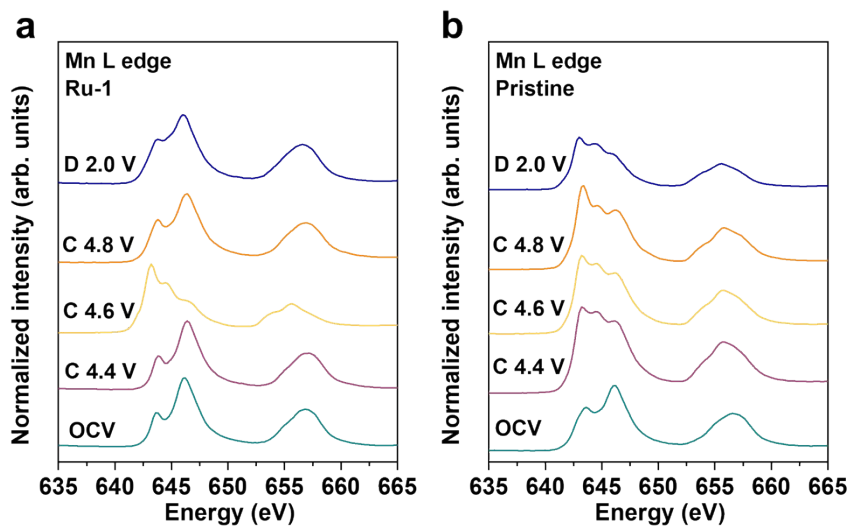


Figure S11 sXAS spectra of Mn L-edge of Ru-1 and pristine sample.

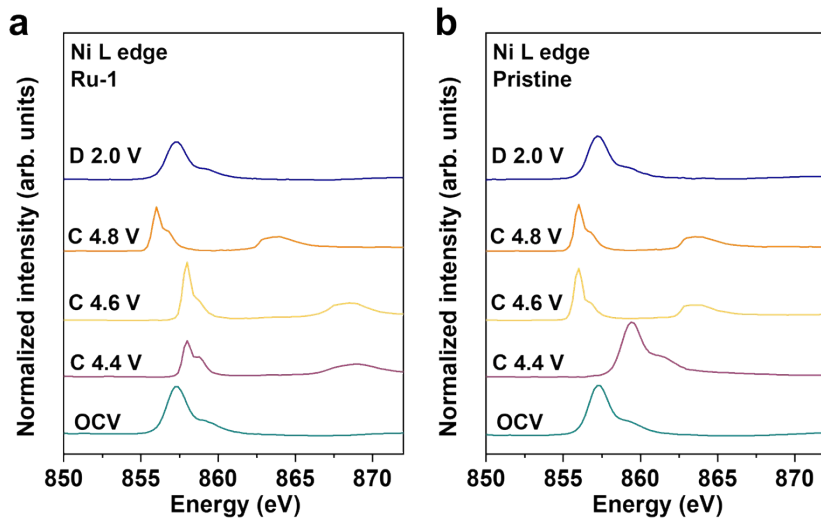


Figure S12 sXAS spectra of Ni L-edge of Ru-1 and pristine sample.

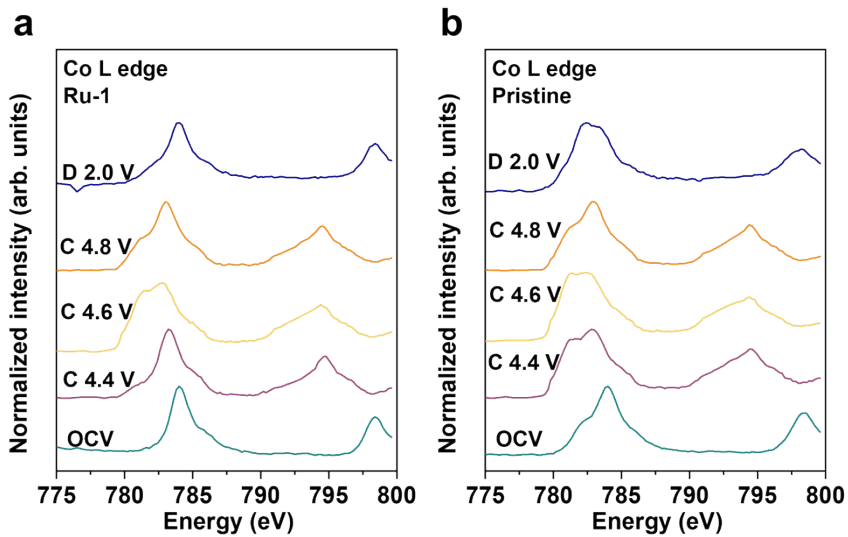


Figure S13 sXAS spectra of Co L-edge of Ru-1 and pristine sample.

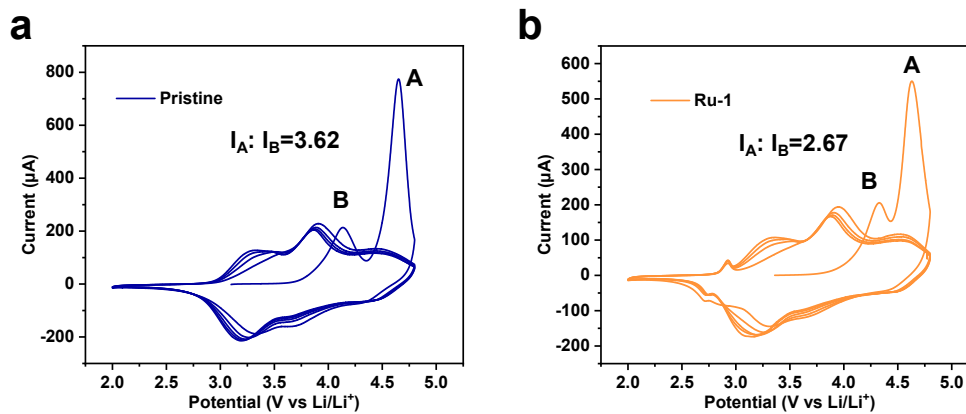


Figure S14 CV curves of (a) pristine sample and (b) Ru-1.

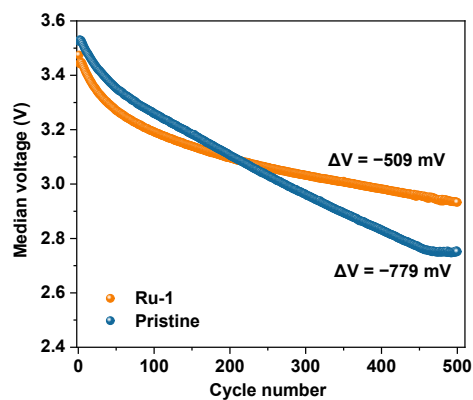


Figure S15 The median voltage decay curves of (a) pristine sample and (b) Ru-1 at a rate of 1 C.

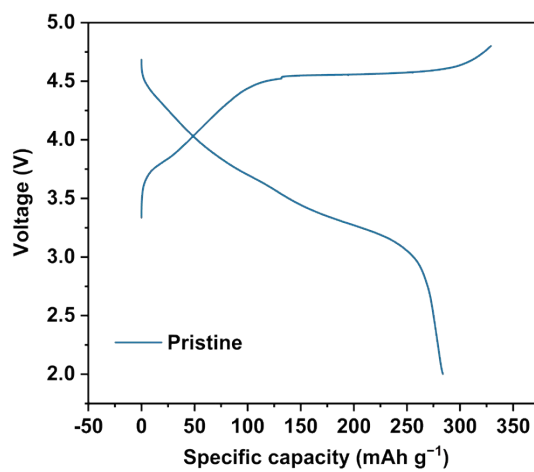


Figure S16 The initial charge and discharge curves of pristine sample.

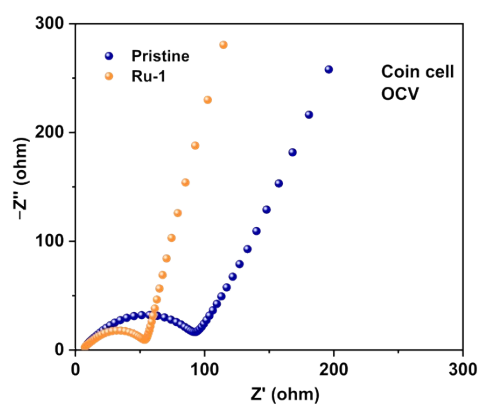


Figure S17 EIS data of Pristine sample and Ru-1 at OCV.

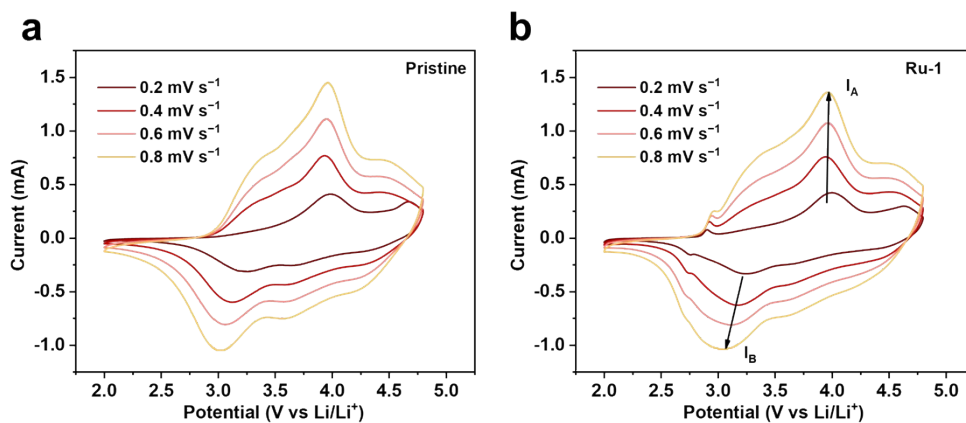


Figure S18 The CV curves of (a) pristine sample and (b) Ru-1 at the rates of 0.2, 0.4, 0.6, and 0.8 mV s⁻¹.

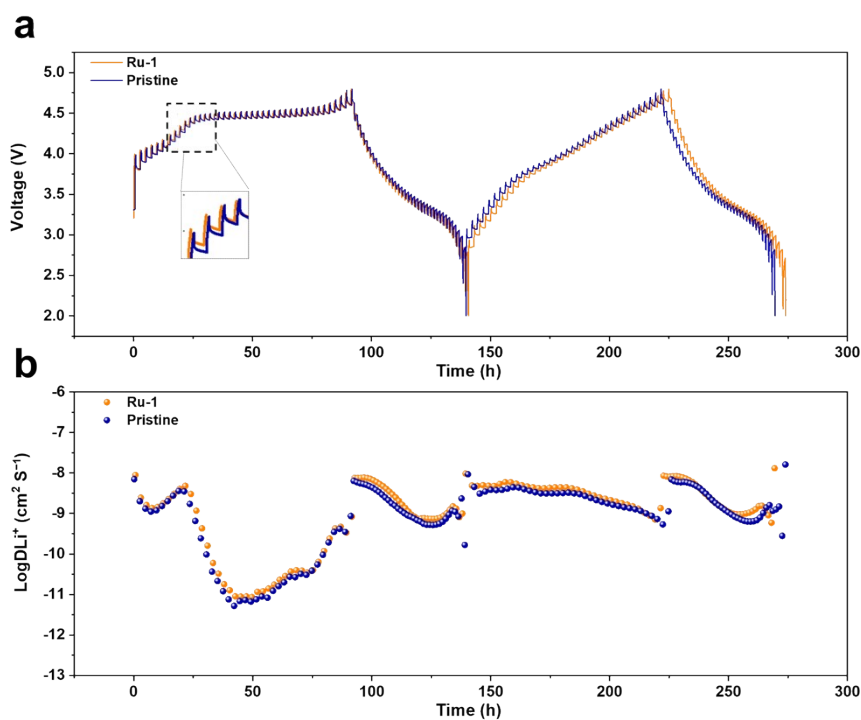


Figure S19 (a) GITT tests for pristine sample and Ru-1, and (b) the corresponding Li⁺ diffusion coefficients.

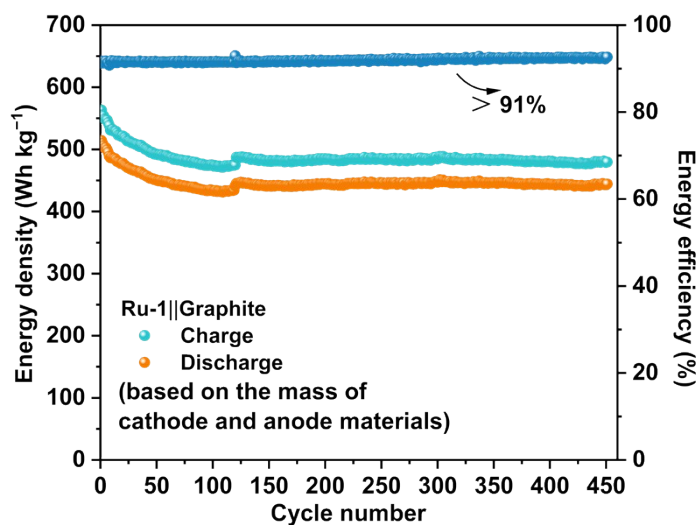


Figure S20 Long-term cycling performance of Ru-1||Graphite pouch cell (the energy density was calculated based on the mass of the cathode material).

a

| DChg. Cap. (Ah) | DChg. Energy(Wh) | Med. Volt. (V) |
|-----------------|------------------|----------------|
| 5.8397 | 19.0007 | 3.4557 |



Figure S21 (a) The screenshot of the Ru-1||Li test results (discharge capacity, discharge energy, and discharge median voltage) captured from Neware battery test software. The optical images of **(b)** the pouch cell weight and **(c)** the pouch cell size measurements.

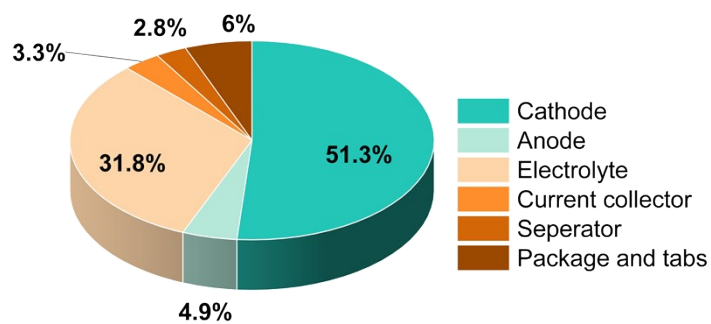


Figure S22 The mass distributions of all components in Ru-1||Li pouch batteries.

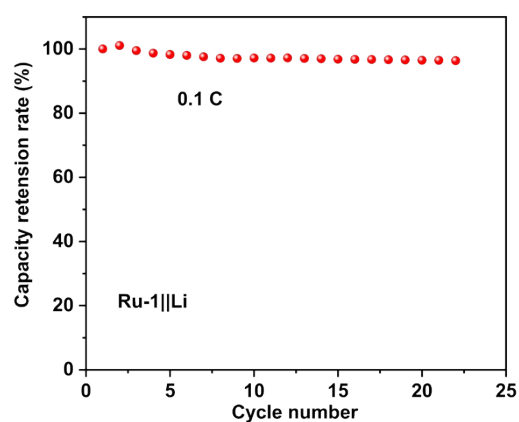


Figure S23 Cycling performance of Ru-1||Li pouch battery.

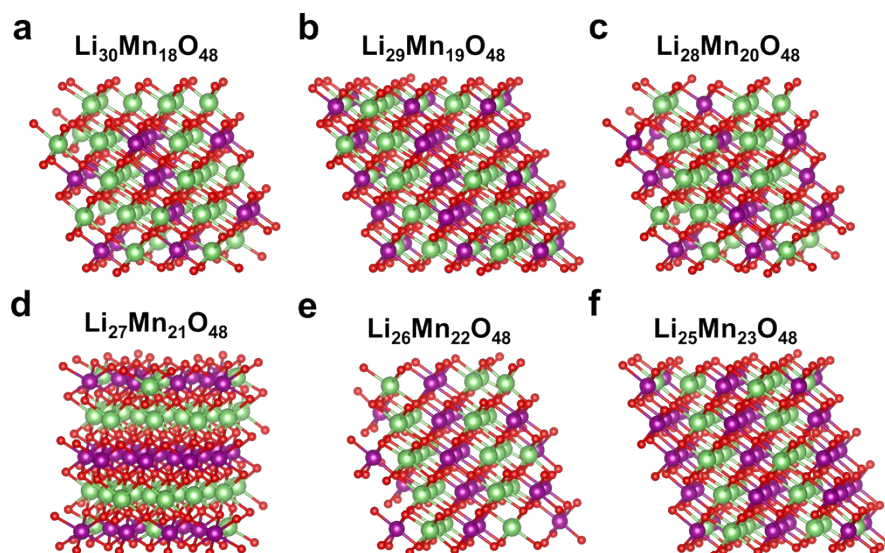


Figure S24 (a-f) Models of $\text{Li}_{30}\text{Mn}_{18}\text{O}_{48}$, $\text{Li}_{29}\text{Mn}_{19}\text{O}_{48}$, $\text{Li}_{28}\text{Mn}_{20}\text{O}_{48}$, $\text{Li}_{27}\text{Mn}_{21}\text{O}_{48}$, $\text{Li}_{26}\text{Mn}_{22}\text{O}_{48}$, and $\text{Li}_{25}\text{Mn}_{23}\text{O}_{48}$ for DOS calculation.

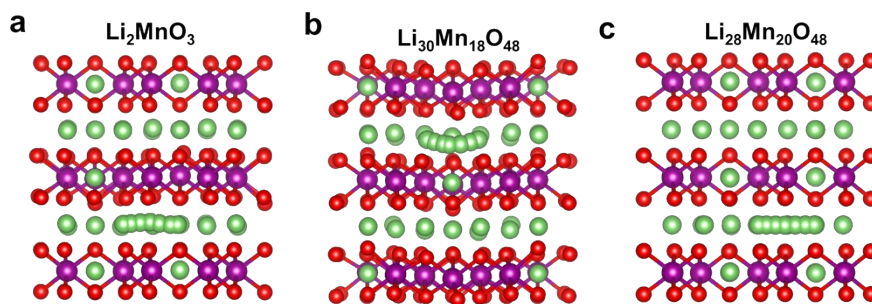


Figure S25 (a-c) Li^+ diffusion models within the Li layer of $\text{Li}_30\text{Mn}_{18}\text{O}_{48}$, $\text{Li}_30\text{Mn}_{18}\text{O}_{48}$, and $\text{Li}_{28}\text{Mn}_{20}\text{O}_{48}$ for Li^+ diffusion energy barrier calculation.

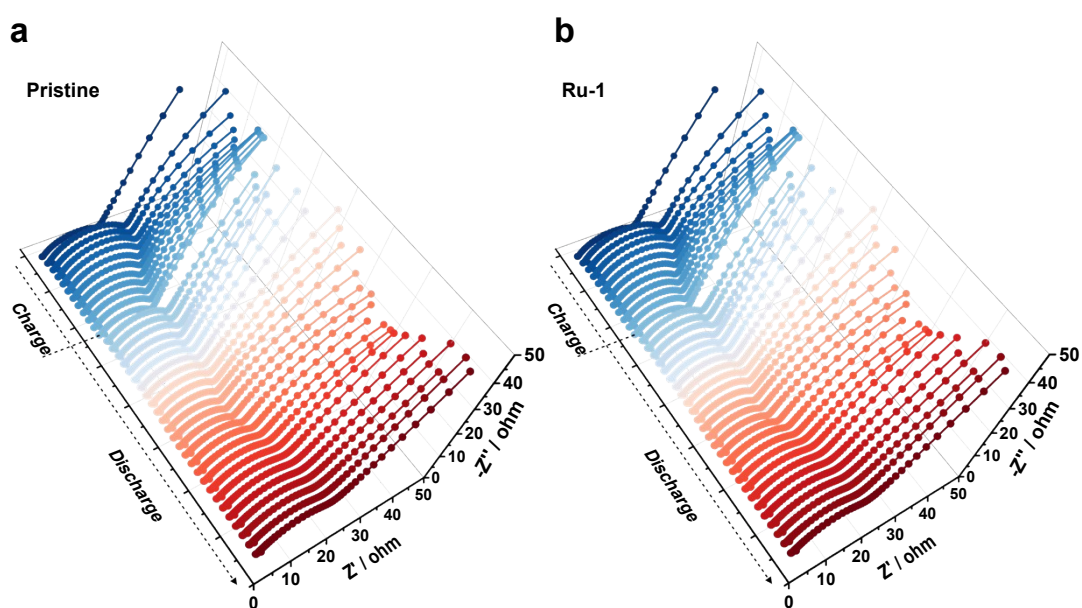


Figure S26 In situ galvanostatic electrochemical impedance spectra (GEIS) of (a) pristine sample and (b) Ru-1.

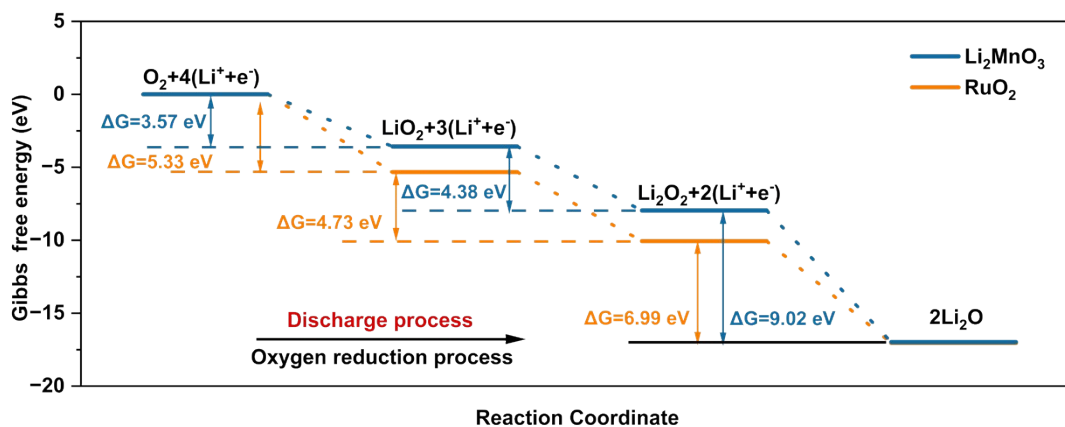


Figure S27 Gibbs free energy pathways of O_2 on Li_2MnO_3 and RuO_2 during the discharge process.

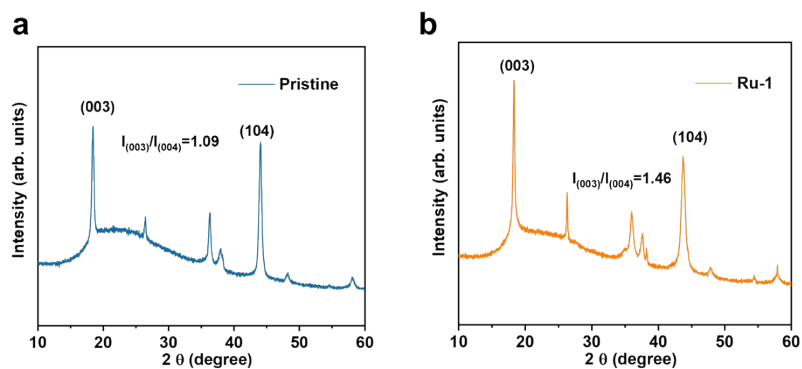


Figure S28 XRD patterns for (a) pristine sample and (b) Ru-1 after 200 cycles.

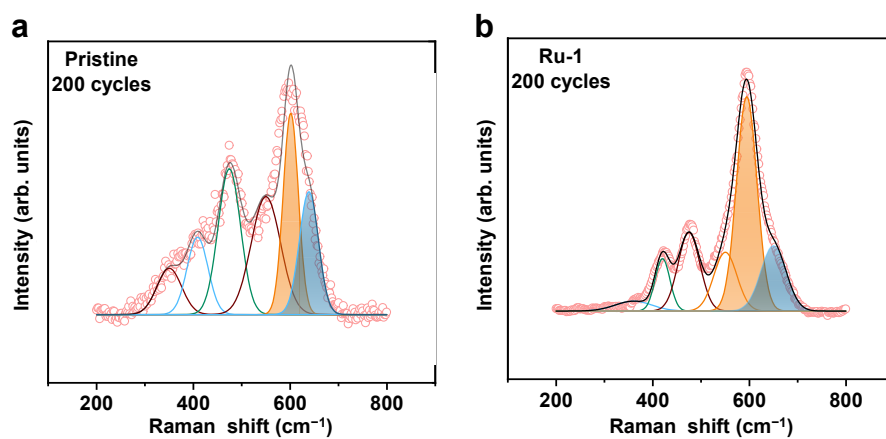


Figure S29 Raman spectra for (a) pristine sample and (b) Ru-1 after 200 cycles.

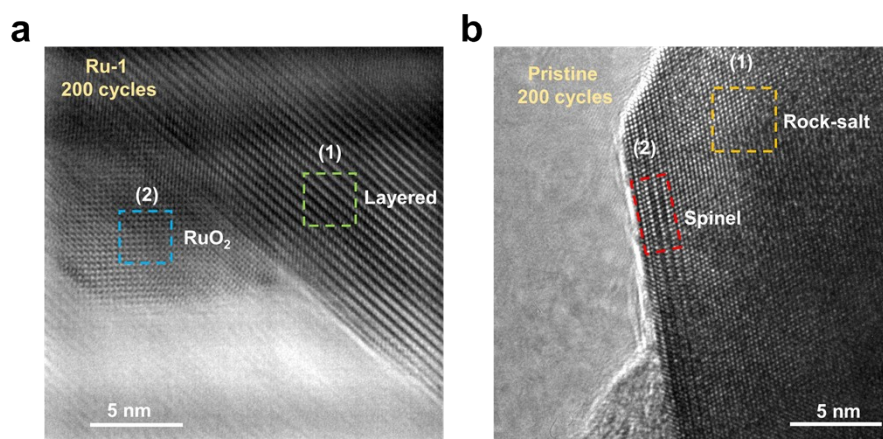


Figure S30 HRTEM images for (a) Ru-1 and (b) pristine sample after 200 cycles.

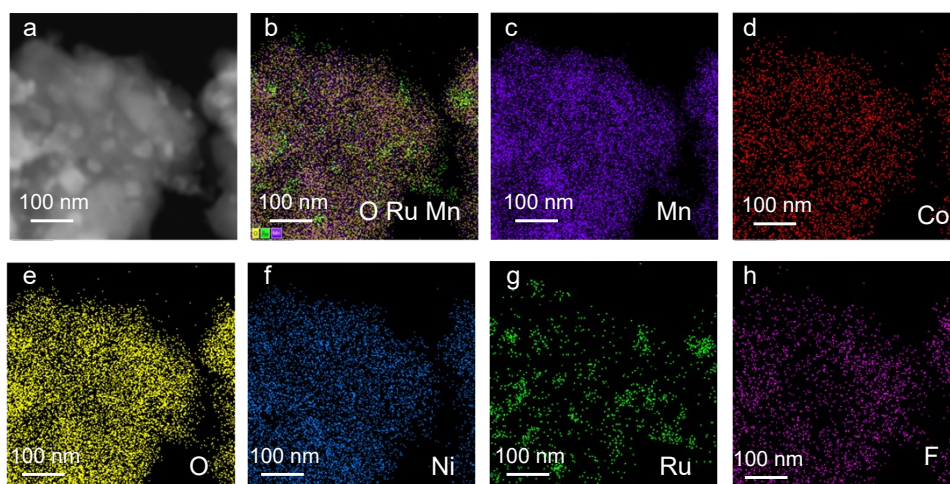


Figure S31 TEM EDS images of Ru-1 after 200 cycles. (a) STEM image of Ru-1. Elements distribution of (b) O, Ru, and Mn, (c) Mn, (d) Co, (e) O, (f) Ni, (g) Ni, and (h) F.

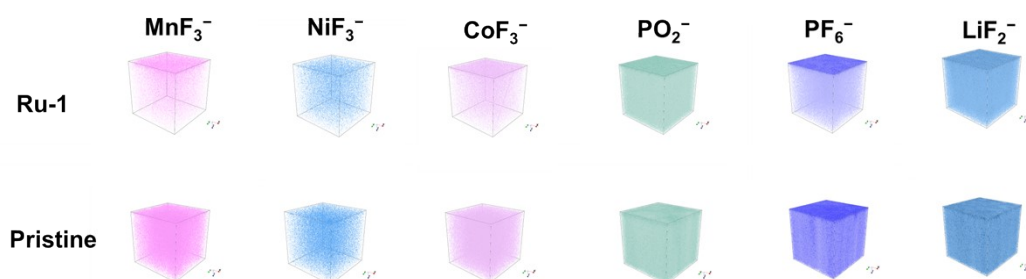


Figure S32 TOF-SIMS three-dimension depth images of the MnF_3^- , NiF_3^- , CoF_3^- , PO_2^- , PF_6^- and LiF_2^- species in Ru-1 and pristine samples after 200 cycles.

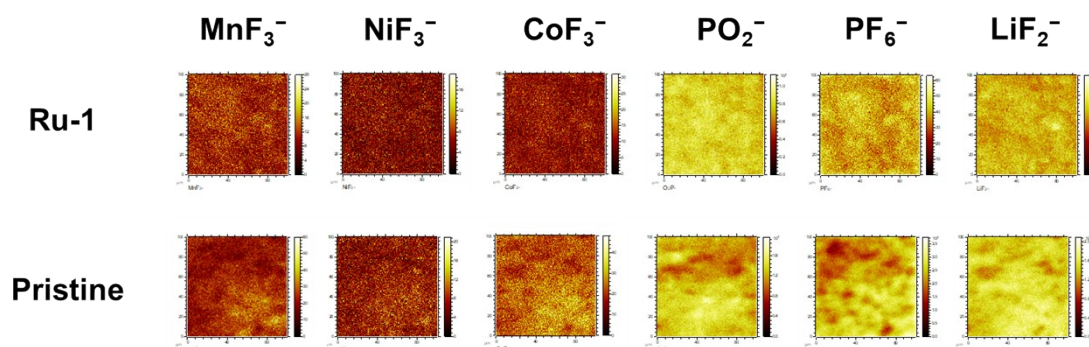


Figure S33 TOF-SIMS two-dimension overlay mapping images of the MnF_3^- , NiF_3^- , CoF_3^- , PO_2^- , PF_6^- and LiF_2^- species in Ru-1 and pristine samples after 200 cycles.

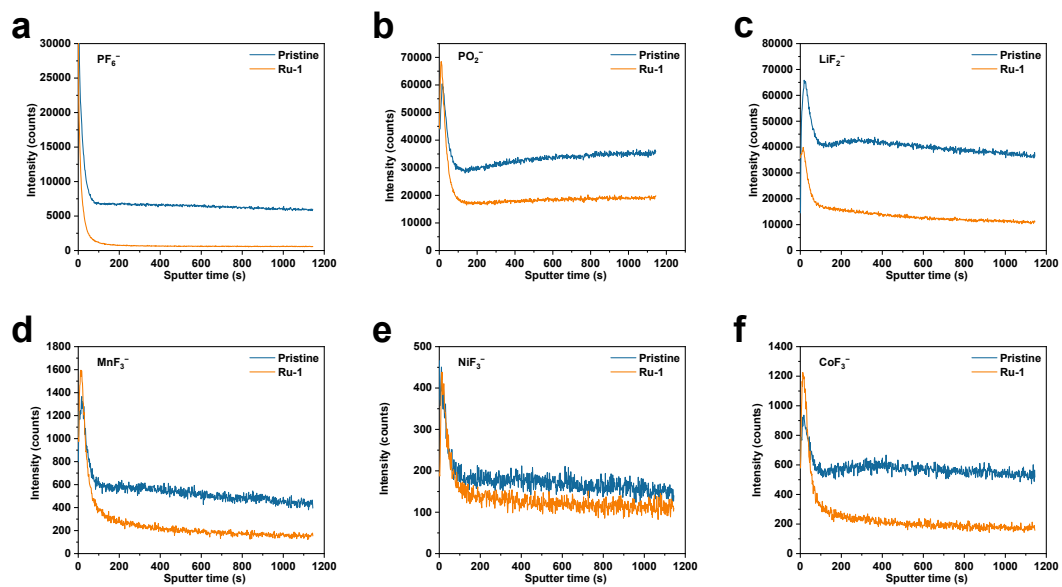


Figure S34 TOF-SIMS depth curves of the MnF_3^- , NiF_3^- , CoF_3^- , PO_2^- , PF_6^- and LiF_2^- species in Ru-1 and pristine samples after 200 cycles.

Supplementary Tables

Table S1 ICE, specific discharge capacities (0.1 C), and capacity retention rates at 1 C after 300 cycles for Ru-0.5, Ru-1, and Ru-3.

| Sample | ICE | Specific discharge capacity of 0.1 C (mAh g ⁻¹) | Capacity retention rate at 1 C after 300 cycles |
|---------------|--------|---|---|
| Ru-0.5 | 95.8% | 309 | 96% |
| Ru-1 | 97.1% | 307 | 98% |
| Ru-3 | 100.0% | 285 | 94% |

Table S2 Lattice parameters of pristine sample and Ru-1 derived from Rietveld refinement of XRD.

| Sample | Phase composition | a (Å) | b (Å) | c (Å) | α (°) | β (°) | γ (°) |
|-----------------|--|---------|---------|----------|--------------|-------------|--------------|
| Pristine | Li ₂ MnO ₃ | 4.97458 | 8.52877 | 5.03961 | 90.000 | 109.135 | 90.000 |
| | LiNi _{0.4} Mn _{0.4} Co _{0.2} O ₂ | 2.85093 | 2.85093 | 14.24484 | 90.000 | 90.000 | 120.000 |
| Ru-1 | Li ₂ MnO ₃ | 4.99844 | 8.52378 | 5.03884 | 90.000 | 109.135 | 90.000 |
| | LiNi _{0.4} Mn _{0.4} Co _{0.2} O ₂ | 2.85408 | 2.85408 | 14.24671 | 90.000 | 90.000 | 120.000 |
| | RuO ₂ | 4.49240 | 4.49240 | 3.06574 | 90.000 | 90.000 | 90.000 |

Table S3 ICP-AES data of Ru-1.

| Element | Li | Mn | Ni | Co | Ru |
|-----------------------------|------|-------|-------|-------|----------|
| Stoichiometric ratio | 1.20 | 0.555 | 0.158 | 0.080 | 0.002825 |

Table S4 Calculated chemical formula and the content of RuO₂ in Ru-1.

| Chemical formula | Li_{1.20}Mn_{0.555}Ni_{0.158}Co_{0.080}O₂ | RuO₂ |
|--------------------------|---|------------------------|
| Content (in mass) | 99.54% | 0.46% |

Table S5 Detailed parameters of the 5.83 Ah Ru-1||Li pouch cell.

| Ru-1 Li pouch cell detailed parameters | |
|---|--|
| Mass of cathode (containing 95% Ru-1) | 19.00 g |
| Mass of anode (10 μm Li on 4 μm Cu foil) | 1.80 g |
| Mass of electrolyte (1 M LiPF ₆ EC- EMC) | 11.76 g, E/C ratio = 2.02 g Ah ⁻¹ |
| Mass of current collector (Al foil: 12 μm) | 1.23 g |
| Mass of separator (PE, 12 μm) | 1.02 g |
| Mass of package and tabs | 2.21 g |
| Mass of the pouch cell | 37.02 g |
| Cell capacity | 5.83 Ah |
| Discharge energy | 19.00 Wh |
| Energy density | 513 Wh kg ⁻¹ |

Table S6 Electrochemical performances of Ru-1 and other works reported recently.

| No. | Maximal capacity (mAh g ⁻¹) | 1 C capacity (mAh g ⁻¹) | Capacity retention | Voltage (V) | 1 C current density (mA g ⁻¹) | Reference |
|-------------|---|-------------------------------------|------------------------|------------------|---|--|
| Ru-1 | 307.8, 0.1 C | 260 | 97%, 300 cycles | 2.0-4.8 V | 250 | This work |
| 1 | 282.4, 0.1 C | ~200 | 95.7%, 300 cycles | 2.0-4.8 V | 200 | Adv. Funct. Mater. 2023, 33, 2214775 |
| 2 | 272.8, 0.1 C | 218.4 | 85%, 200 cycles | 2.0-4.8 V | 200 | Adv. Mater. 2020, 32, 1906070 |
| 3 | 303, 0.1 C | 253 | 85%, 200 cycles | 2.1-4.8 V | 200 | Adv. Mater. 2023, 35, 2307138 |
| 4 | ~220, 0.1 C | ~180 | 94.0%, 200 cycles | 2.0-4.6 V | 250 | Adv. Funct. Mater. 2023, 33, 2302236 |
| 5 | 298, 0.2 C | ~240 | 92.5%, 400 cycles | 2.0-4.8 V | 250 | Adv. Funct. Mater. 2023, 33, 2303707 |
| 6 | ~240, 0.2 C | ~180 | 94%, 500 cycles | 2.0-4.8 V | 250 | ACS Appl. Energy Mater. 2021, 4, 11234-11247 |
| 7 | ~250, 0.1 C | ~210 | 82%, 200 cycles | 2.0-4.7 V | 250 | Energy Storage Mater. 2020, 32, 37-45 |
| 8 | ~280, 0.1 C | 215 | 74%, 500 cycles | / | / | Angew. Chem. Int. Ed. 2023, 62, e202213806 |
| 9 | 292, 0.1 C | 213.5 | 85.4%, 100 cycles | 2.0-4.8 V | 250 | Small 2023, 19, 2303539 |
| 10 | ~270, 0.1 C | ~230 | 84.70%, 100 cycles | 2.0-4.8 V | 200 | Adv. Mater. 2024, 36, 2303612 |
| 11 | 254, 0.1 C | 173.1 | 86.4%, 300 cycles | 2.0-4.8 V | 250 | Angew. Chem. Int. Ed. 2021, 60, 23248-23255 |
| 12 | 303.8, 0.1 C | 257.2 | 93.6%, 100 cycles | 2.0-5.0 V | 200 | Angew. Chem. Int. Ed. 2020, 59, 23061-23066 |
| 13 | 278.2, 0.1 C | 231.8 | 91.8%, 400 cycles | 2.0-4.8 V | / | Angew. Chem. Int. Ed. 2022, 61, e202203698 |
| 14 | ~300, 0.1 C | ~220 | 93.6%, 100 cycles | 2.1-4.8 V | 250 | Adv. Mater. 2023, 35, 2208726 |
| 15 | 307.8, 0.1 C | 245.7 | 91.5%, 200 cycles | 2.1-4.8 V | 250 | Adv. Mater. 2022, 34, 2109564 |
| 16 | 273.6 | 239.1 | 91.96%, 200 cycles | 2.0-4.8 V | 200 | Chem. Eng. J. 2023, 465, 142928 |

Table S7 Maximum strain of pristine sample and Ru-1 calculated by COMSOL.

| Charging time (h) | Strain of Pristine sample (MPa) | Strain of Ru-1 sample (MPa) |
|-------------------|---------------------------------|-----------------------------|
| 0.16 | 567 | 418 |
| 0.18 | 427 | 351 |

Reference

1. Perdew JP, Burke K, Ernzerhof M. Generalized Gradient Approximation Made Simple. *Physical Review Letters* **77**, 3865-3868 (1996).
2. Kresse G, Furthmüller J. Efficient iterative schemes for ab initio total-energy calculations using a plane-wave basis set. *Physical Review B* **54**, 11169-11186 (1996).
3. Anisimov VI, Zaanen J, Andersen OK. Band theory and Mott insulators: Hubbard U instead of Stoner I. *Physical Review B* **44**, 943-954 (1991).
4. Seo D-H, Lee J, Urban A, Malik R, Kang S, Ceder G. The structural and chemical origin of the oxygen redox activity in layered and cation-disordered Li-excess cathode materials. *Nature Chemistry* **8**, 692-697 (2016).
5. Henkelman G, Uberuaga BP, Jónsson H. A climbing image nudged elastic band method for finding saddle points and minimum energy paths. *The Journal of Chemical Physics* **113**, 9901-9904 (2000).